ARTICLE

Check for updates

# Traditional seismic hazard analyses underestimate hazard levels when compared to observations from the 2023 Kahramanmaras earthquakes

Abdullah Altindal [1,2]✉ & Aysegul Askan[1]

A sequence of two major earthquakes, $Mw$7.8 Pazarcik, and $Mw$7.5 Elbistan, struck Southeastern Turkey in February 2023. The large magnitudes of the earthquakes and the short time between the two events raised questions about whether this sequence was an extremely rare disaster. Here, based on prior knowledge, we perform seismic hazard assessment for the region to estimate exceedance probabilities of observed magnitudes and ground motions. We discuss that many regional studies indicated the seismic gap in the area but with lower magnitude estimations. Observed ground motions generally agree with empirical models for the Pazarcik event. However, some records with high amplitudes exceed the highest observed amplitudes in an extensive database of shallow crustal earthquakes. We observe a notable trend of residuals for the Elbistan earthquake, leading to underestimation at long periods. We discuss potential advances in science for better characterization of such major earthquakes in the future.

[1] Middle East Technical University, Ankara, Turkey. [2] Present address: Swiss Seismological Service (SED) at ETH Zurich, Zurich, Switzerland.
✉email: abdullah.altindal@sed.ethz.ch

On 6 February 2023, two large magnitude earthquakes struck Southeastern Turkey with moment magnitudes (Mw) of 7.8 and 7.5, with epicenters located near the Pazarcik and Elbistan districts of Kahramanmaras province, respectively. The combined effects of the two earthquakes were felt in a very large area, including most of Turkey and Syria. The region did not previously experience any major earthquakes in the instrumental era. However, the high seismic hazard was very well known due to the historical seismicity and the large number of active faults in the region. The major historical earthquakes include the 1513 Turkoglu, 1822 Aleppo, 1872 Amik Lake, and 1893 Malatya earthquakes, with estimated surface-wave magnitudes (Ms) of 7.4, 7.4, 7.2, and 7.1, respectively[1]. The region is located at the intersection of three major tectonic plates (i.e., Anatolian, Arabian, and African plates), resulting in a complex and dense faulting[2]. The largest active faults in the region are segments of the East Anatolian Fault Zone (EAFZ) and Dead Sea Fault Zone (DSFZ). The details about these fault zones, including their segmentation, can be found in Duman and Emre[3] and Emre et al.[4].

The locations of the two earthquakes were not surprising. Many studies pointed out the high seismic potential of the southern end of the EAFZ, implying a seismic gap near Kahramanmaras, inferred from the relatively low seismicity and the long time elapsed since the latest major earthquakes in the region[3,5–7]. However, estimates of the maximum magnitude in the region were generally smaller, as both earthquakes ruptured multiple fault segments. In Fig. 1, surface projections of the fault ruptures of the two earthquakes, obtained from the finite-fault models of the United States Geological Survey[8] are shown in comparison to the corresponding fault segments in Southeastern Turkey obtained from Emre et al.[4]. It can be observed that the rupture of the Mw7.8 earthquake corresponds to five segments shown in Emre et al.[4]. Two segments, Narli and Sakcagoz, are mapped as parts of the DSFZ; whereas the remaining three, Amanos, Pazarcik, and Erkenek, are mapped as parts of the EAFZ. The rupture of the Mw7.5 earthquake, on the other hand, corresponds to two segments of the Surgu Fault Zone (SFZ) and the Cardak fault.

Emre et al.[4] also give estimates of the maximum magnitude for each segment, as shown in the legend of Fig. 1b, while noting that their estimates are specific to each segment, and multi-segment ruptures should be considered in seismic hazard assessment as well. While performing probabilistic seismic hazard assessment (PSHA) for the same region, Gülerce et al.[9] considered multi-segment ruptures of the Erkenek and Pazarcik segments. They similarly included multi-segment ruptures of both segments of the SFZ in their analyses. Using GPS data, Aktug et al.[7] calculated the slip rates along the EAFZ and estimated the seismic potential near the Pazarcik segment as Mw7.7. Most recently, Güvercin et al.[5] studied the seismotectonics of EAFZ and provided estimates of maximum magnitudes and return periods for several segments of EAFZ. They estimated a maximum magnitude of 7.3 for the Pazarcik segment with a return period of 700 years and a maximum magnitude of 7.4 with a return period of 900 years for the Amanos segment. Overall, the combined ruptures of the Pazarcik and Amanos segments were not anticipated in the literature, as most studies provided separate estimates for the maximum magnitudes.

This study attempts to provide a quantitative discussion into the question of whether this earthquake sequence was an extremely rare disaster or not. Since the question itself is a highly subjective one, and perhaps open to speculation, we focus on parameters associated with the earthquake sequence for which reliable empirical prediction models exist in the literature. In order to avoid speculation, we provide quantitative estimates for

the probability of exceedance values for the magnitude of the earthquakes and amplitudes of the observed ground motion levels. To obtain quantitative estimates of return periods of the fault ruptures and the observed ground motion levels, PSHA is performed for the locations of the seismic stations that recorded at least one of the two mainshocks. The recorded ground motions are also compared to predictive ground motion models (GMMs) to assess how extreme the observations are relative to the observed earthquake fault ruptures (i.e., the probability of observing ground motion levels at least as extreme as the recorded motions, conditional on the observed earthquake magnitudes and fault ruptures).

## Recorded ground motions

The dataset of recorded ground motions for the two earthquakes is obtained from Gülerce et al.[10], where they used the raw ground acceleration data published by the Disaster and Emergency Management Presidency of Turkey (AFAD). They eliminated potentially problematic records (i.e., records with incomplete trace, considerable noise content, or an unclear trace of the event) and processed the remaining records according to the procedure described in Akkar et al.[11]. Since this study focuses primarily on ground motions with relatively high amplitudes, only the records within 100 km of the fault plane are considered. In addition, the records at stations where the time-averaged shear-wave velocity within the upper 30 meters ($V_{S30}$) is unknown are also eliminated, as this site proxy is a key input to GMMs. This resulted in 51 records for the Mw7.8 Pazarcik event and 25 records for the Mw7.5 Elbistan event. For all records, three ground motion intensity measures are calculated: peak ground acceleration (PGA) and 5% damped elastic spectral acceleration at periods of 0.5 and 1.0 seconds ($SA_{T=0.5s}$ and $SA_{T=1.0s}$). These three parameters are selected to roughly account for the variations in the frequency content of the ground motions. The RotD50 value for all intensity measures is calculated from the two orthogonal horizontal components. For two horizontal and orthogonal components, the RotD50 value is calculated by rotating the ground motion at small increments to get the acceleration at various orientations; calculating the intensity measure for each orientation; and calculating the median intensity across all orientations[12]. Figures 2 and 3 show the spatial distribution of the calculated intensity measures (i.e., PGA, $SA_{T=0.5s}$, and $SA_{T=1.0s}$) for the Mw7.8 Pazarcik and Mw7.5 Elbistan earthquakes, respectively. The locations of the stations with respect to the fault planes are also presented as a zipped Keyhole Markup Language (.kmz) file, along with key information on the records and stations in Supplementary Data 1.

## Probabilistic seismic hazard assessment for the region

PSHA is a mathematical framework based on the total probability theorem for estimating the exceedance rates of intensity measure levels. This section provides a brief and simplified overview of the methodology without intending to provide a complete picture. A detailed explanation of the method, underlying assumptions, as well as recent developments can be found in Baker et al.[13].

The mathematical equation for estimating the exceedance rate of a given intensity measure level (also called the seismic hazard integral) is expressed as follows[13–15]:

$$\lambda(IM > im) = \sum_{j=1}^{n_{sources}} \sum_{i=1}^{n_{rup_j}} P\left(IM > im | rup_{i,j}, site\right) \lambda\left(rup_{i,j}\right) \quad (1)$$

where IM is the considered intensity measure (e.g., PGA), im is the considered level of IM (e.g., 1 g), $\lambda(IM > im)$ is the occurrence rate of observing IM values greater than im, $rup_{i,j}$ is an individual fault rupture i at seismic source j, $\lambda(rup_{i,j})$ is the estimated rate of
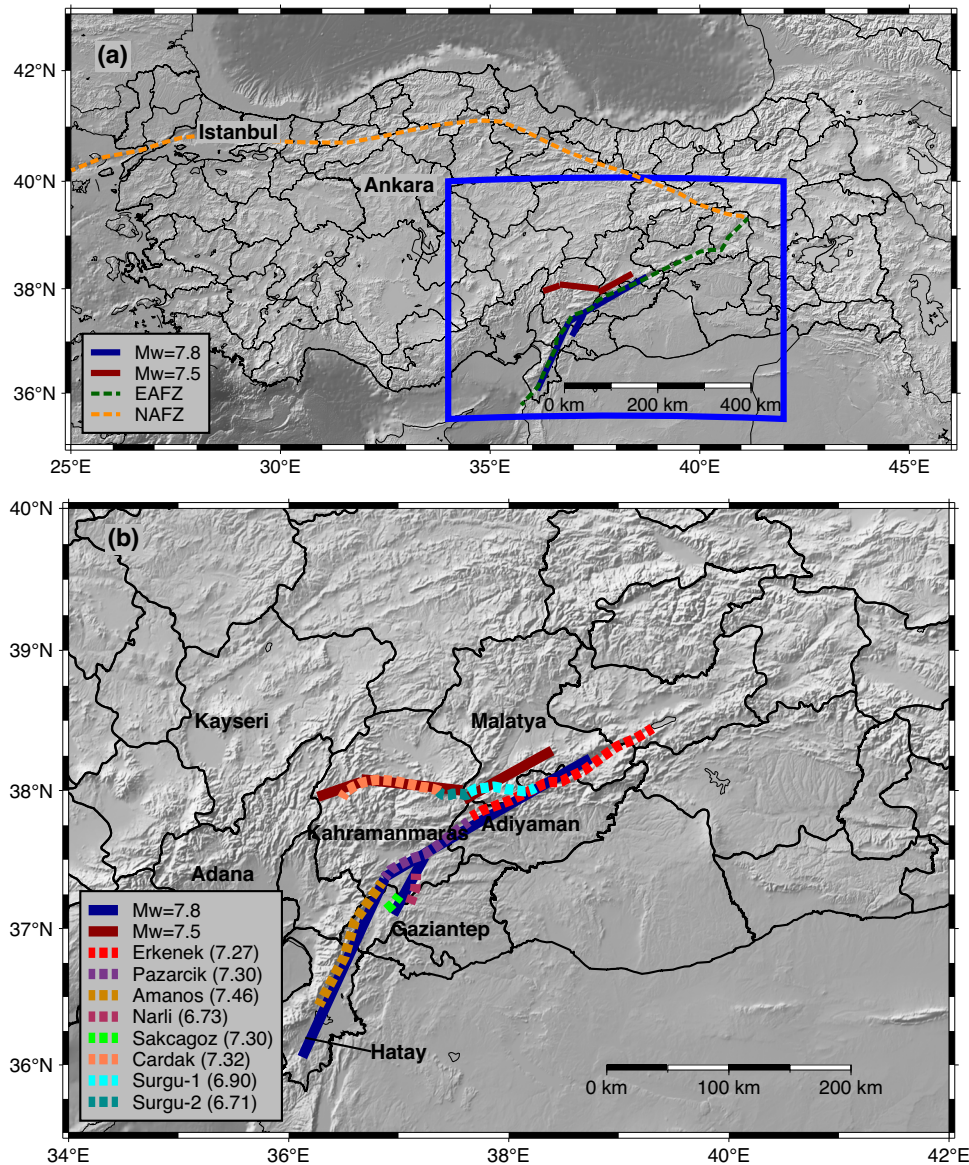
**Fig. 1 Comparison of the observed fault ruptures to the active fault map of Turkey. a** Surface projection of fault ruptures for 6 February earthquakes, along with the simplified traces of EAFZ and NAFZ **b** Surface projection of fault ruptures for 6 February earthquakes in comparison to segmentation of active fault map of Turkey[4]. The surface projections of the fault ruptures are obtained from the finite-fault models of the United States Geological Survey[8]. A blue rectangle in **a** indicates the selected frame in **b**. The estimated maximum magnitude for each segment is shown in parentheses in the legend of **b**.

rupture $i$ at the source $j$, and $P\left(IM > im | rup_{i,j}, site\right)$ is the probability of observing an $IM$ value greater than $im$ at the considered *site* given that the considered rupture $rup_{i,j}$ takes place. By summing over all considered seismic sources in the region, and all potential ruptures in each seismic source, Eq. (1) estimates the total rate of exceeding $im$ by considering the contributions from each seismic source in the region. Repeating Eq. (1) for many $im$ values and plotting the exceedance rates against $im$ values result in the most common output of PSHA, called the hazard curve. An example hazard curve for *PGA*, constructed for station 3125, located in Antakya, Hatay, is shown in Fig. 4.

Equation (1) can be separated into two components. The first one is the conditional probability of exceeding $im$, i.e., $P(IM > im | rup_{i,j}, site)$, at the site of interest, given an earthquake rupture $rup_{i,j}$. This part of the equation is most commonly calculated through empirical GMMs by assuming normally distributed model residuals[16]. Most empirical GMMs take the following

simplified functional form to estimate the natural logarithm of intensity measures, $\ln IM$[13]:

$$\ln IM = \mu_{\ln IM}\left(rup, site\right) + \sigma_{\ln IM}\left(rup, site\right) \times \epsilon \quad (2)$$

where $\mu_{\ln IM}\left(rup, site\right)$ is the median prediction, $\sigma_{\ln IM}\left(rup, site\right)$ is the total standard deviation of the model, and $\epsilon$ is a standard normal random variable with a zero mean and unit standard deviation, expressing the difference between observation and median prediction as the number of standard deviations. $P\left(IM > im | rup_{i,j}, site\right)$ can then be calculated as:

$$P\left(IM > im | rup_{i,j}, site\right) = 1 - \phi\left(\frac{\ln im - \mu_{\ln IM}\left(rup, site\right)}{\sigma_{\ln IM}\left(rup, site\right)}\right) \quad (3)$$

where $\phi$ is the cumulative distribution function of the standard normal distribution. Equation (3) can also be expressed as a
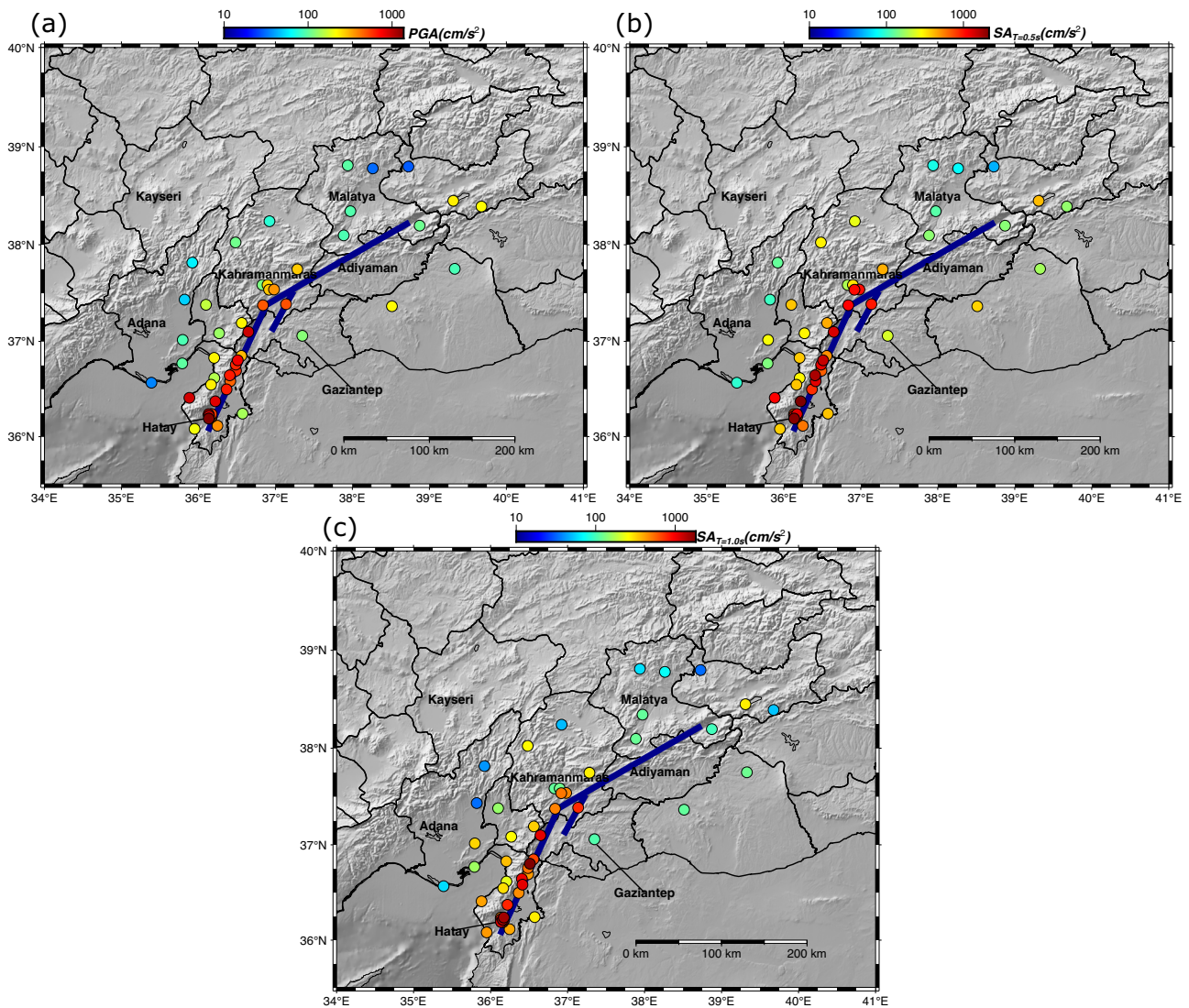
**Fig. 2 Maps of recorded ground motion intensities for the *Mw*7.8 Pazarcik earthquake.** Maps show intensities in terms of **a** peak ground acceleration, *PGA*, **b** spectral acceleration at a period of 0.5 s, $SA_{T=0.5s}$, **c** spectral acceleration at a period of 1.0 s, $SA_{T=1.0s}$.

function of the normalized residual $\epsilon$ as:

$$P\left(IM > im | rup_{i,j}, site\right) = 1 - \phi(\epsilon) \qquad (4)$$

The second component is the occurrence rates of the considered earthquake ruptures, $\lambda(rup_{i,j})$. An individual earthquake rupture can be generally defined with an estimate of the total released energy (seismic moment, $M_0$, or moment magnitude, $Mw$) and the fault geometry. The rates of earthquakes exceeding a given magnitude are generally estimated with magnitude-frequency distributions (MFD). The most common MFDs used in practice are the double truncated Gutenberg-Richter[17] and characteristic earthquake models[18], both of which are modifications to the original Gutenberg-Richter model[19], which has the following form:

$$\log_{10} N(M > m) = a - b \times m \qquad (5)$$

where $N(M > m)$ is the number of earthquakes with a magnitude $M$ greater than $m$, and $a$ and $b$ are the parameters of the Gutenberg-Richter MFD. The $a$-value describes the overall seismic activity of the region, whereas the $b$-value describes the proportion of small-magnitude earthquakes to large-magnitude earthquakes. Both double truncated Gutenberg-Richter and

characteristic earthquake models impose a maximum magnitude ($M_{max}$) to the classical Gutenberg-Richter relationship to eliminate very large magnitudes that are considered physically impossible. The characteristic earthquake model also assumes an increased probability of a so-called characteristic magnitude and magnitudes in its vicinity. The value of the characteristic magnitude is usually determined through historical evidence for the large-magnitude earthquakes at a given fault. On the other hand, a double truncated Gutenberg-Richter model introduces an upper bound magnitude ($M_{max}$) and a minimum considered magnitude ($M_{min}$) to the classical Gutenberg-Richter model while preserving the exponential decay.

This study uses publicly available inputs of the European Seismic Hazard Model 2020, ESHM20[20] to perform PSHA at each seismic station shown in Figs. 2 and 3. PSHA calculations are performed with the open-source OpenQuake platform[21]. Instead of using the already available seismic hazard curves computed in ESHM20, we compute site-specific curves in order not to be limited by the spatial resolution of the original model, which is designed for a continental scale.

The source model of ESHM20 includes area and fault source models for the Euro-Mediterranean region. To capture the epistemic uncertainty in the inputs of MFDs, the logic tree shown in
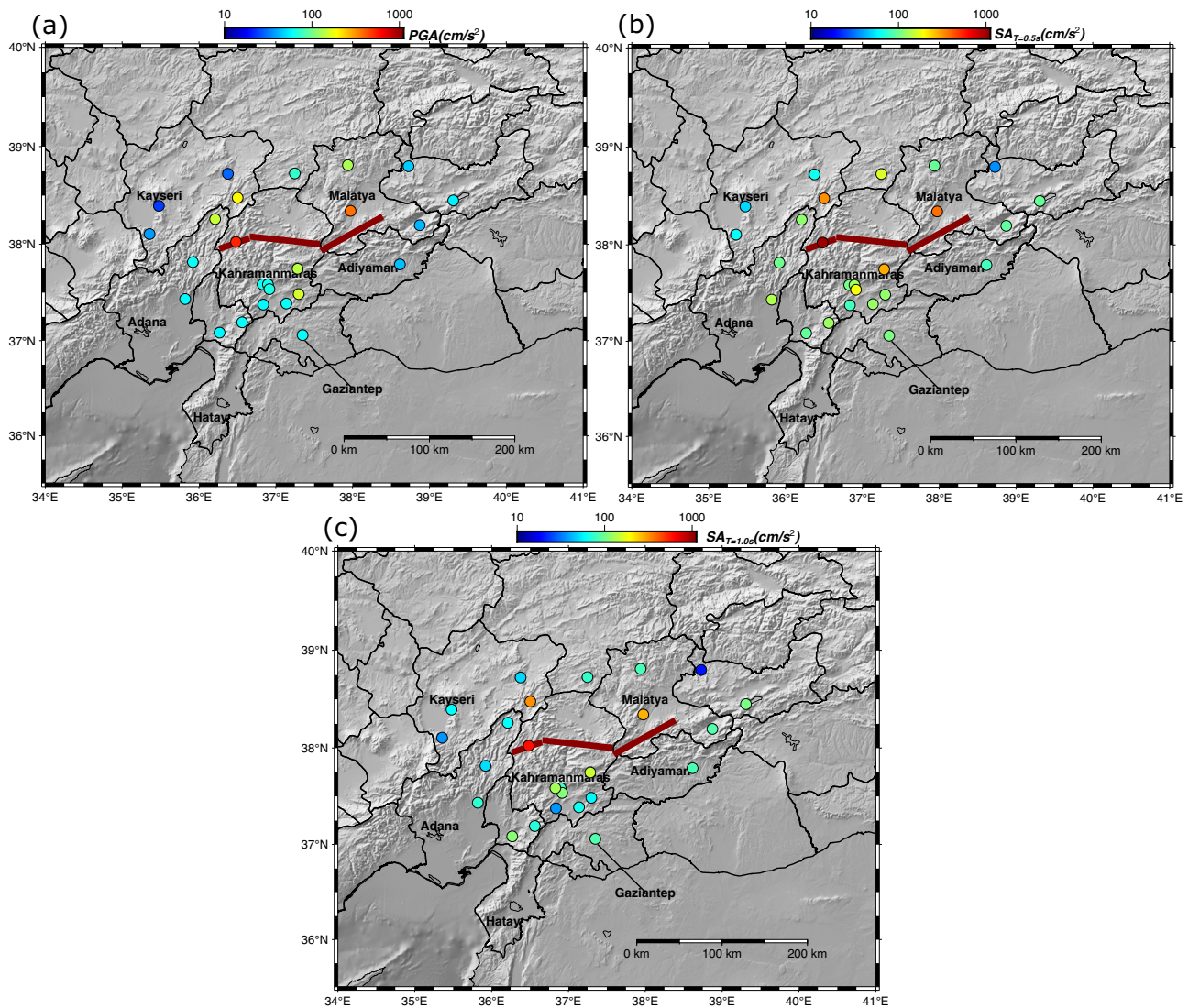
**Fig. 3 Maps of recorded ground motion intensities for the *Mw*7.5 Elbistan earthquake.** Maps show intensities in terms of **a** peak ground acceleration, *PGA*, **b** spectral acceleration at a period of 0.5 s, $SA_{T=0.5s}$, **c** spectral acceleration at a period of 1.0 s, $SA_{T=1.0s}$.
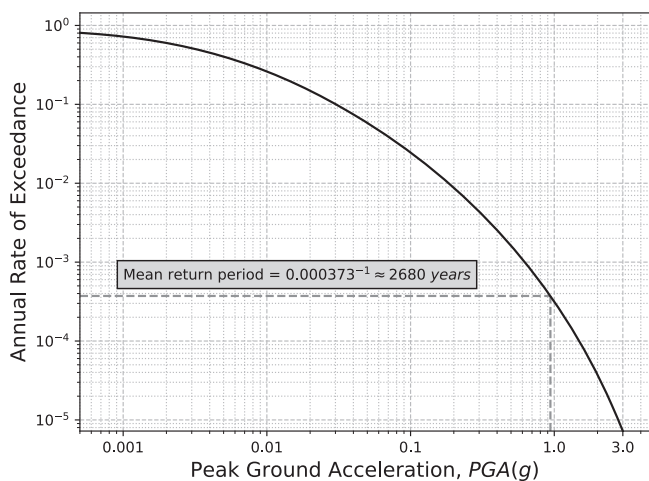


**Fig. 4 An example hazard curve for *PGA*, constructed for station 3125 located in Antakya, Hatay.** Calculation of the mean return period for the observed *PGA* level of 0.94 g is also illustrated.

Fig. 5 is used. Here, in addition to the common double truncated Gutenberg-Richter MFD, a tapered Pareto distribution[22,23] with median *a* and *b* values is also used in a single branch with a weight of 0.4 for area sources. For the other branch of the area source model, a double truncated Gutenberg-Richter MFD is used with three further branches. These three branches combine the 5th, 50th (i.e., median), and 95th percentile values for a and b values with weights of 0.2, 0.6, and 0.2, respectively. The three a and b values are not exhaustively permutated as these combinations would correspond to extreme cases with non-trivial weights[20]. For the fault models, a single *b* value for the tectonic region is used, along with three different values for slip rate, as it was observed that the *b*-value uncertainties were less important in resulting MFDs when compared to the slip rate and $M_{max}$ uncertainties. The slip rates are compiled from the European Fault-Source Model 2020[24]. The slip rates are converted to activity rates assuming moment conservation.

Maximum magnitudes for area sources in ESHM20 are estimated based on prior seismic activity. The lower bound of maximum magnitude ($M_{max\,1}$) is set equal to the highest observed magnitude for the zone, increased by one standard deviation. The
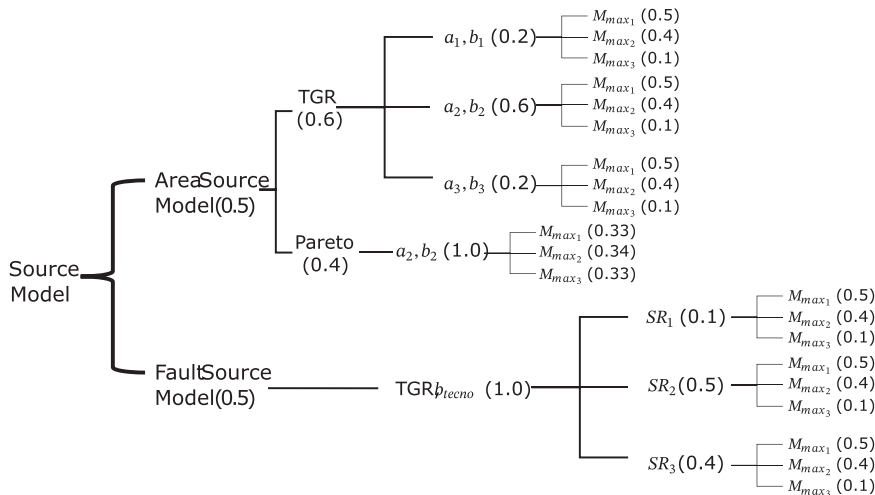
**Fig. 5 The source model logic tree of ESHM20 for shallow crustal earthquakes.** The subscripts 1, 2, and 3 represent the lower bound, median, and upper bound values for the inputs, respectively. TGR stands for double truncated Gutenberg Richter MFD, and SR stands for slip rate. $b_{tecno}$ is the median $b$ value for the tectonic region.
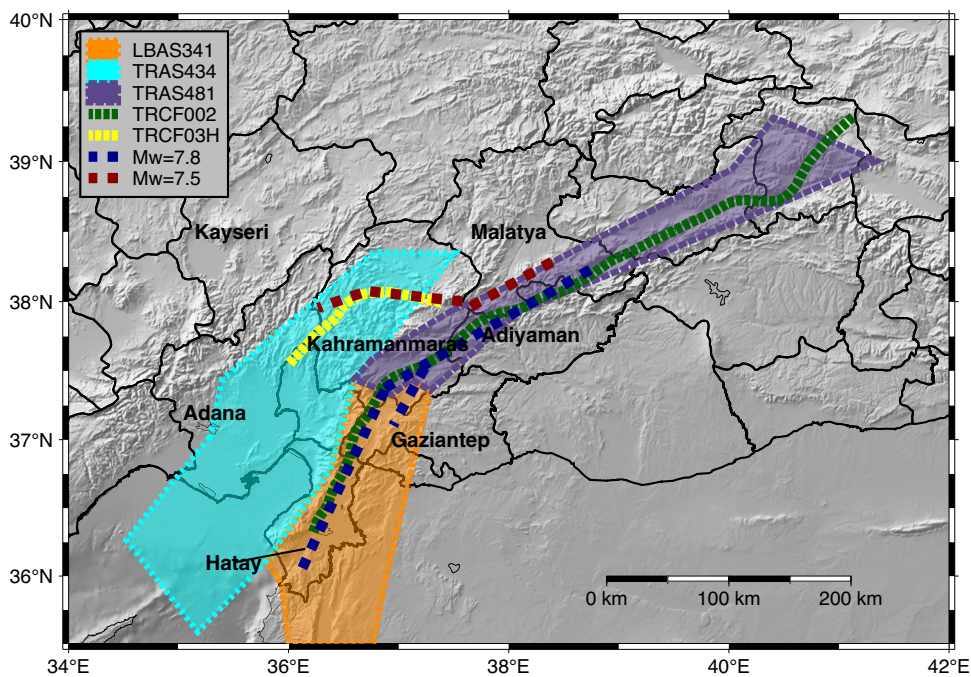


**Fig. 6 Area and fault sources in the source model of the European Seismic Hazard Model, ESHM20 that correspond to the fault ruptures of the *Mw*7.8 Pazarcik and *Mw*7.5 Elbistan earthquakes.** The rupture of the *Mw*7.8 Pazarcik earthquake coincides with two area sources, TRAS481 and LBAS341, and one fault source, TRCF002. The rupture of the *Mw*7.5 Elbistan earthquake coincides with one area source, TRAS434, and one fault source, TRCF03H.

median ($M_{max\,2}$) and upper bound ($M_{max\,3}$) magnitudes are determined by adding a magnitude increment of 0.3 and 0.6, respectively. This value of 0.3 is the standard deviation of earthquake magnitude estimated from the entire unified catalog of ESHM20. The maximum magnitudes for fault sources are estimated with the fault scaling law of Leonard[25]. For each site-specific PSHA calculation, seismic sources within a 200 km distance are considered. The locations of the area and fault sources in the source model of ESHM20 that coincide with the observed ruptures of the Kahramanmaras earthquakes are shown in Fig. 6, and the key parameters of these source models are shown in Table 1. In summary, the approach of ESHM20 for estimating the maximum magnitudes of seismic sources is based on a combination of prior major seismic activity, as well as the scaling of

magnitudes with the fault rupture area[25]. For the area sources, maximum magnitudes are estimated considering the highest observed magnitudes in the region and the catalog uncertainty. For the fault models, the maximum magnitudes are estimated based on the magnitude scaling with the fault rupture area. These two approaches are combined in the final seismic hazard estimates through the logic tree shown in Fig. 5 with a total of 21 branches.

The ground motion characterization of ESHM20 is based on the scaled backbone logic tree approach, where a single GMM is calibrated with various adjustment factors to capture epistemic uncertainties in the seismological properties of the region. For the backbone model, the partially non-ergodic GMM of Kotha et al.[26,27] is used, which has the following functional form for

**Table 1 Key parameters of the area and fault sources in the source model of the European Seismic Hazard Model, ESHM20, that corresponds to the fault ruptures of the *Mw*7.8 Pazarcik and *Mw*7.5 Elbistan earthquakes.**

| Source Name | Source Type | $M_{max}$ | | | a-values | | | b-values | | | $b_{tecto}$ | Slip rate (mm/year) | | |
|---|---|---|---|---|---|---|---|---|---|---|---|---|---|---|
| | | $M_{max1}$ | $M_{max2}$ | $M_{max3}$ | $a_1$ | $a_2$ | $a_3$ | $b_1$ | $b_2$ | $b_3$ | | SR1 | SR2 | SR3 |
| LBAS341 | Area | 7.7 | 8.0 | 8.3 | 3.38 | 3.45 | 3.52 | 0.76 | 0.80 | 0.84 | 0.98 | - | - | - |
| TRAS481 | Area | 7.7 | 8.0 | 8.3 | 3.90 | 3.95 | 4.00 | 0.83 | 0.87 | 0.91 | 0.98 | - | - | - |
| TRAS434 | Area | 7.7 | 8.0 | 8.3 | 4.77 | 4.80 | 4.83 | 1.01 | 1.05 | 1.09 | 0.98 | - | - | - |
| TRCF002 | Fault | 8.1 | 8.5 | 9.1 | - | - | - | - | - | - | 0.98 | 5.40 | 7.15 | 8.90 |
| TRCF03H | Fault | 7.5 | 7.9 | 8.2 | - | - | - | - | - | - | 0.98 | 2.00 | 2.50 | 3.00 |

the median predictions:

$$\overline{\ln IM}_{e,l,s,r} = \ln \mu + \delta B^0_{e,l} + \delta L2L_l + \delta S2S_s + \delta c_{3,r} \qquad (6)$$

where $\overline{\ln IM}_{e,l,s,r}$ is the median prediction, and subscripts of $e$, $l$, $s$, and $r$ stand for the event, tectonic locality, site, and region, respectively. In Eq. (6), $\ln\mu$ describes the fixed-effect prediction without any adjustments for the event, tectonic locality, site, or region. $\delta B^0_{e,l}$, $\delta L2L_l$, $\delta S2S_s$, and $\delta c_{3,r}$ are the random-effect adjustments for the event, tectonic locality, site, and region, respectively. The fixed-effect prediction, $\ln\mu$, is described as follows:

$$\ln \mu = e_1 + f_{R,g}(M_w, R_{JB}) + f_{R,a}(R_{JB}) + f_M(M_w) \qquad (7)$$

where $e_1$ is the generic offset term, $f_{R,g}(M_w, R_{JB})$ is the geometric spreading function, $f_{R,a}(R_{JB})$ is the anelastic attenuation function, and $f_M(M_w)$ is the source function, representing the magnitude scaling of motion. $R_{JB}$ is the most common source-to-site distance metric used in GMMs, defined as the distance to the surface projection of the fault.

The derivation of the logic tree used in the ground motion characterization of ESHM20 is described in Weatherill et al.[28] and Weatherill and Cotton[29]. Using the described inputs of ESHM20, hazard curves for $PGA$, $SA_{T=0.5s}$, and $SA_{T=1.0s}$ are generated for the seismic stations in our dataset with the Open-Quake Engine platform.

## Results

**Magnitude-frequency distributions**. The fault source model of ESHM20 is not finely segmented unlike most regional seismic source characterization studies (e.g., Emre et al.[3]). Hence, the entire EAFZ is modeled as a single fault source (TRCF002) with a total length of 576 km which almost completely encompass the observed fault rupture of 350 km for the *Mw*7.8 Pazarcik earthquake. The *Mw*7.5 Elbistan earthquake occurred on a relatively less studied fault structure which is potentially mapped with lower accuracy compared to the EAFZ, resulting in a moderate disagreement between the fault model of ESHM20 and the observed rupture (Fig. 6). In particular, the northeast extension of the fault zone (Surgu-1) is not mapped in the fault source model of ESHM20 within the TRCF03H fault. However, the total length of the TRCF03H and the observed rupture are quite similar as the TRCF03H fault further extends towards the southwest. When the agreement between the area source model of ESHM20 and the observed fault ruptures are investigated, it is observed that the rupture of the *Mw*7.8 earthquake is not confined to a single area source, but it has substantial portions in two: LBAS341 and TRAS481. Similarly, the observed rupture of the *Mw*7.5 Elbistan earthquake corresponds to two area sources, TRAS434 and TRAS481, although most of the rupture is within TRAS434.

Initially, MFDs for the sources of ESHM20 are investigated to estimate the probability of observing earthquakes with magnitudes larger than or equal to 7.8 and 7.5 at sources

coinciding with the ruptures of Pazarcik and Elbistan earthquakes, respectively. MFDs corresponding to different logic tree branches (Fig. 5) are combined by calculating a weighted average with the same weights from the logic tree. The estimated annual rates are converted to mean return periods for easier interpretation, as shown in Fig. 7.

For the *Mw*7.8 Pazarcik earthquake, the mean return period is estimated as about 1000 years with the fault source model, TRCF002, which resembles the observed fault rupture very similarly towards the southern end (Fig. 6). The two area sources in the same region, TRAS481, and LBAS341, yield mean return period estimates of about 4000 and 3500 years, respectively. For the *Mw*7.5 Elbistan earthquake, the mean return period is estimated as about 7800 years with the corresponding fault source, TRCF03H, and 2600 years, with the corresponding area source, TRAS434.

**Mean return periods of observed ground motion amplitudes**. For each station in the compiled dataset, mean return periods for the observed levels of three parameters, $PGA$, $SA_{T=0.5s}$, and $SA_{T=1.0s}$ are calculated from the hazard curves calculated in the previous section. Calculation of the mean return period for the observed $PGA$ level of 0.94 g at station 3125 located in Antakya, Hatay, is illustrated in Fig. 4. Spatial distributions of estimated mean return periods are shown in Figs. 8 and 9 for the *Mw*7.8 Pazarcik and *Mw*7.5 Elbistan earthquakes, respectively. Estimated return periods and corresponding observed ground motion levels are shown in Fig. 10 for both earthquakes. The maximum estimated return periods for exceeding the observed ground motion levels during the *Mw*7.8 Pazarcik earthquake are approximately 6900, 4100, and 6900 years for $PGA$, $SA_{T=0.5s}$, and $SA_{T=1.0s}$, respectively. Maximum estimates for the *Mw*7.5 Elbistan earthquake are 1200, 1700, and 6900 years for $PGA$, $SA_{T=0.5s}$, and $SA_{T=1.0s}$, respectively. Figure 10 also displays the 16th and 84th percentile return period estimates among all individual logic tree branches. Here, it is observed that the estimates are highly variable and sensitive to logic tree branches. The variability is most prominent for very high return periods, especially for the upper limit of the confidence interval.

**Comparison of recorded ground motions to GMMs**. The recorded ground motions can also be compared to GMMs with inputs constrained to represent the observed fault rupture and subsurface conditions at the site of interest. Although the GMM of Kotha et al.[26,27] was used for the PSHA in the previous section, the GMM of Boore et al. was preferred for the residual analyses performed in this section, as the dataset of Boore et al.[30] contains earthquakes with magnitudes as large as 7.9. However, the maximum magnitude earthquake used in the derivation of the Kotha et al.[26,27] model was 7.4, which is lower than the magnitudes of both earthquakes analyzed in this study. The residuals at vibration periods between 0.01 and 10 seconds for the ground motions of both earthquakes are shown in Fig. 11 according to
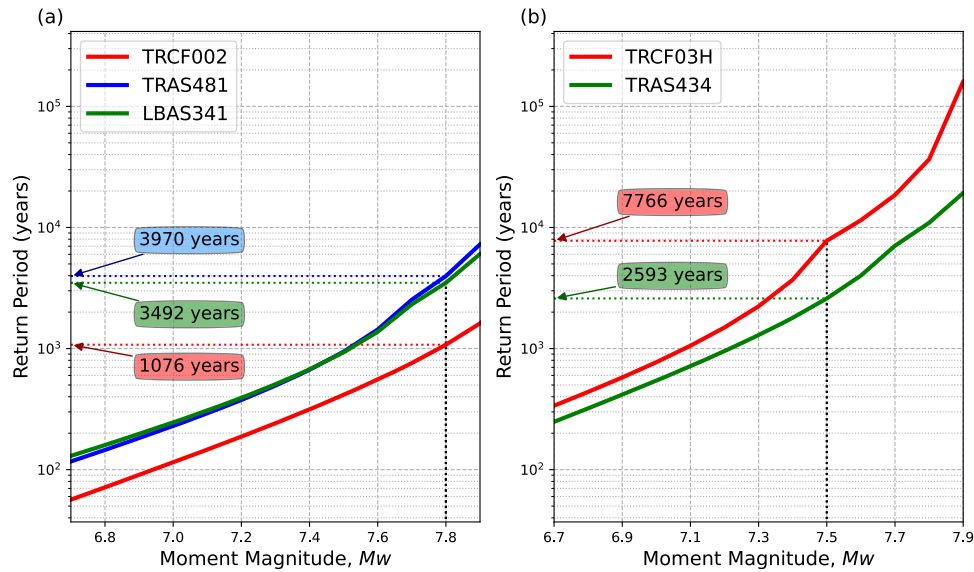
**Fig. 7 Mean return periods for the observed earthquake magnitudes of 7.8 and 7.5. a** Mean return period of a *Mw*7.8 earthquake at the sources coinciding with the rupture of the Pazarcik earthquake. **b** Mean return period of a *Mw*7.5 earthquake at the sources coinciding with the rupture of the Elbistan earthquake. Mean return periods are calculated for both area and fault sources of ESHM20. In both figures, the individual return periods estimated for a single branch of the logic tree are also plotted against magnitude.

Boore et al.[30] model. Since it is a standard normal variable, the $\epsilon$ values can also be interpreted as the probability of exceeding the observed levels of ground motion, conditional on the observed earthquake rupture and the known subsurface conditions (i.e., $V_{S30}$). The corresponding percentile values for $\epsilon$ values are also given in parentheses in Fig. 11. The residuals for the recorded motion at station 3135, located in Arsuz, Hatay, are observed to be generally high across all periods, with a maximum value of about 3 (corresponding to a probability of exceedance of only 0.1%) at a period of 0.3 seconds. A more in-depth investigation of this record is provided in Fig. 12. Here, the elastic response spectra of the observed motion are compared to the 475- and 2475-year return period design spectra described in the Turkish Building Earthquake Code[31] and Boore et al.[30]. It is observed that the recorded motion generally exceeds both code provisions and model predictions in almost the entire period range. Figure 12 also presents ground acceleration and velocity series, as well as the Fourier spectrum of the recorded motion. The station is in the forward directivity region and located very close to the fault rupture (Fig. 12b), therefore, the motion is expected to be considerably affected by the finite-fault effects. The high amplitudes and relatively short duration of the motion also support the potential forward directivity effects. However, when the velocity trace of the record is investigated (Fig. 12e), no clear pulse-like features are observed.

One peculiar thing about this ground motion record is its broadband nature, with very high amplitudes across all vibration periods. The probability of observing such broadband motions can be approximated through the multivariate normal distribution for two or more vibration periods, as spectral accelerations at multiple periods are well approximated by a joint normal distribution[32]. For simplicity, two periods are selected for this analysis as 0.3 and 3.0 seconds to represent shorter and longer periods, respectively. The period of 0.3 seconds is selected as the period of maximum residual, and 3.0 seconds is selected as a period of high positive residual, which is also further away from 0.3 seconds so that the correlation between the two vectors of residuals is not very high. The observed residuals at these two periods are 2.96 and 1.21 (Fig. 12). The correlations between spectral acceleration values at different vibration periods are

estimated with the correlation model of Baker and Jayaram[33]. This model is preferred even though it was derived from an older version of the NGA database, as the correlation estimates are shown to be insensitive to the choice of GMM[33]. This model predicts a correlation of 0.2535 for GMM residuals at periods of 0.3 and 3.0 seconds. Using this information, the probability of observing a ground motion that is at least as extreme as the observed motion at periods of 0.3 and 3.0 seconds is calculated as follows:

$$\Pr\left(\epsilon_{T=0.3s} \ge 2.96 \; \epsilon_{T=3.0s} \ge 1.21 \Big| \rho_{\epsilon_{T=0.3s},\epsilon_{T=3.0s}} = 0.2535\right) \approx 0.0005 (1 \, in \, 2000)$$
(8)

For completeness, the same probability is calculated for periods of 0.5 and 1.0 seconds, as these periods were used prior to summarize the observed ground motions. The correlation between the residuals for these two periods is 0.749, calculated with the model of Baker and Jayaram[33]. The observed residuals at 0.5 and 1.0 seconds are 2.19 and 1.70, respectively. Consequently, the probability of observing a ground motion that is at least as extreme as the observed motion at periods of 0.5 and 1.0 seconds is calculated as follows:

$$\Pr\left(\epsilon_{T=0.5s} \ge 2.19 \; \epsilon_{T=1.0s} \ge 1.70 \Big| \rho_{\epsilon_{T=0.5s},\epsilon_{T=1.0s}} = 0.749\right) \approx 0.0086 (1 \, in \, 116)$$
(9)

These low probabilities indicate that the observed high amplitudes are not localized peaks, but the recorded motion at this station is considerably higher than expectations within the entire period range. The low probabilities and high residuals calculated in this section might indicate that the observed ground motions are much higher than the expected levels for such large-magnitude earthquakes. However, the employed GMMs are derived from datasets that lack records from such large-magnitude earthquakes recorded very close to the fault ruptures. In fact, the records of this earthquake sequence will likely lead to updates of existing empirical models, especially for constraining the scaling of motions with larger magnitudes at short source-to-site distances.
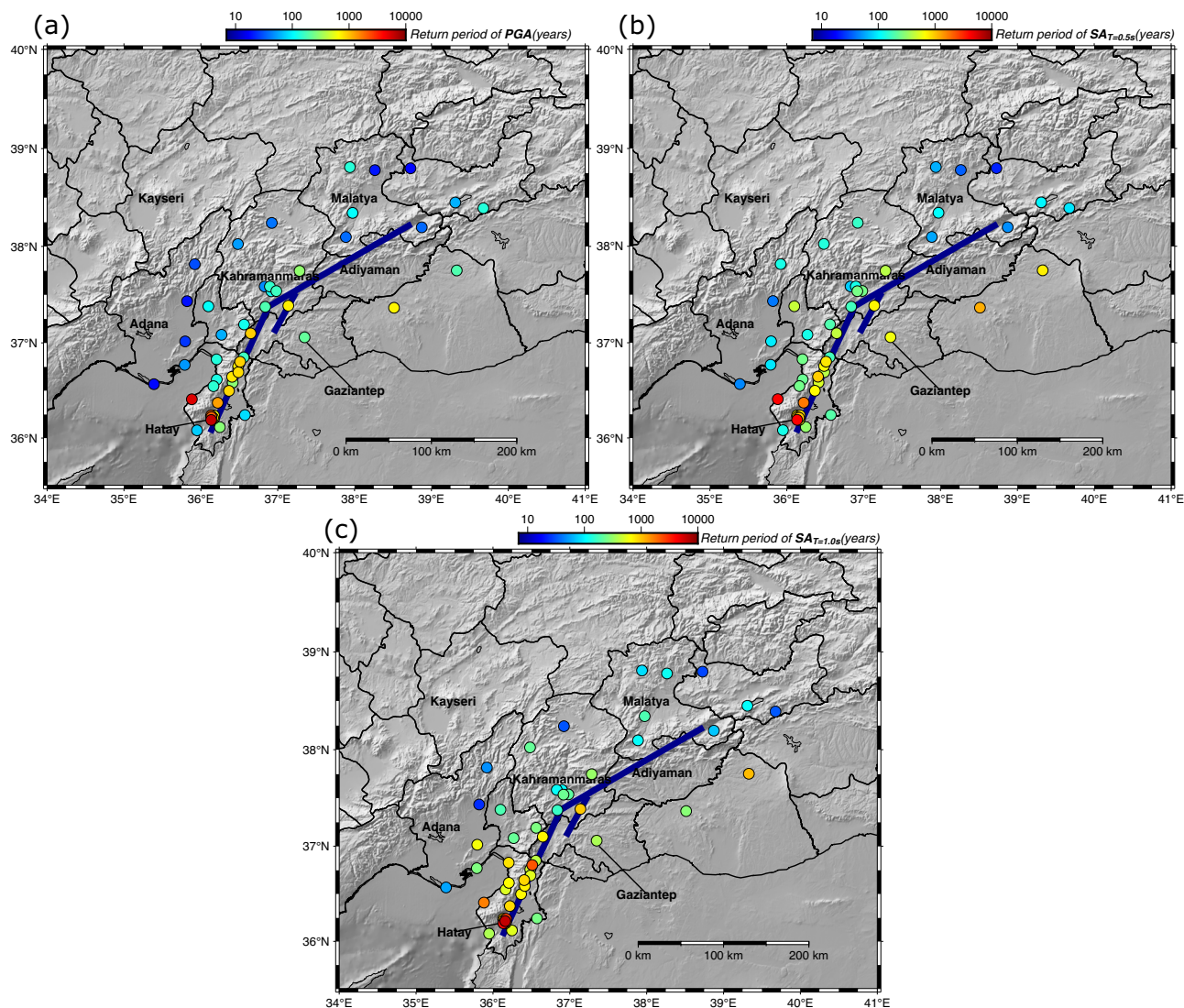
**Fig. 8 Maps showing the calculated mean return periods for the observed ground motion levels during the *Mw*7.8 Pazarcik Earthquake.** Maps show return periods of **a** *PGA*, **b** $SA_{T=0.5s}$, **c** $SA_{T=1.0s}$ for the *Mw*7.8 Pazarcik earthquake.

**Comparison of recorded ground motions to previous recordings**. This section compares the recorded ground motions from the two earthquakes to some of the most extreme ground motions in the NGA-West2 database[34], containing more than 20,000 records from 599 shallow crustal earthquakes in active tectonic regimes. Records from the NGA-West2 database with the highest spectral acceleration values at discrete periods between 0.01 and 10 seconds are identified for comparison. This selection criterion resulted in 19 unique ground motion records from nine earthquakes, as shown in Table 2. A comparison of the response spectra of these 19 records against five of the records from 6 February 2023 is shown in Fig. 13. Here, four records are selected from the *Mw*7.8 Pazarcik earthquake at stations 3126, 3138, 3139, and 3135. In addition, one record from the *Mw*7.5 Elbistan earthquake at station 4612 is also included in the comparison. It is observed that the selected five records are generally comparable to the maximum values in the entire NGA-West2 database. Particularly, $SA_{T=1.5}$ value at station 3138 (1.20 g) is slightly higher than the maximum value in the NGA-West2 database (1.17 g). Similarly, $SA_{T=1.8}$ value at station 3139 (1.12 g) is shown to be higher than the maximum value in the NGA-West2 database (1.08 g).

## Discussion

The Kahramanmaras earthquake sequence on 6 February 2023 initiated many discussions on whether these earthquakes were anticipated or not. This study offers an investigation of the observed fault ruptures and recorded ground motions to estimate how extreme the two earthquakes are, based on the prior scientific knowledge of the region. The seismic potential of the region was well known, but the maximum magnitude estimates were generally lower than the observed magnitudes of 7.8 and 7.5. In particular, Amanos and Pazarcik segments of EAFZ (Fig. 1b) were generally considered independent fault segments, and a combined rupture of the two segments was not considered in previous regional seismic hazard studies. However, a recent seismic hazard model, ESHM20, modeled most of EAFZ as a single fault source with a length of more than 500 kilometers.

The use of fault sources for seismic hazard assessment is generally preferred over area sources when the seismotectonic structure is well known, and records of prior seismic activity allow precise modeling of fault locations and MFDs. This was indeed the case for the EAFZ, as many studies focused on its geometry, segmentation, slip rate, and seismic potential[3–7].
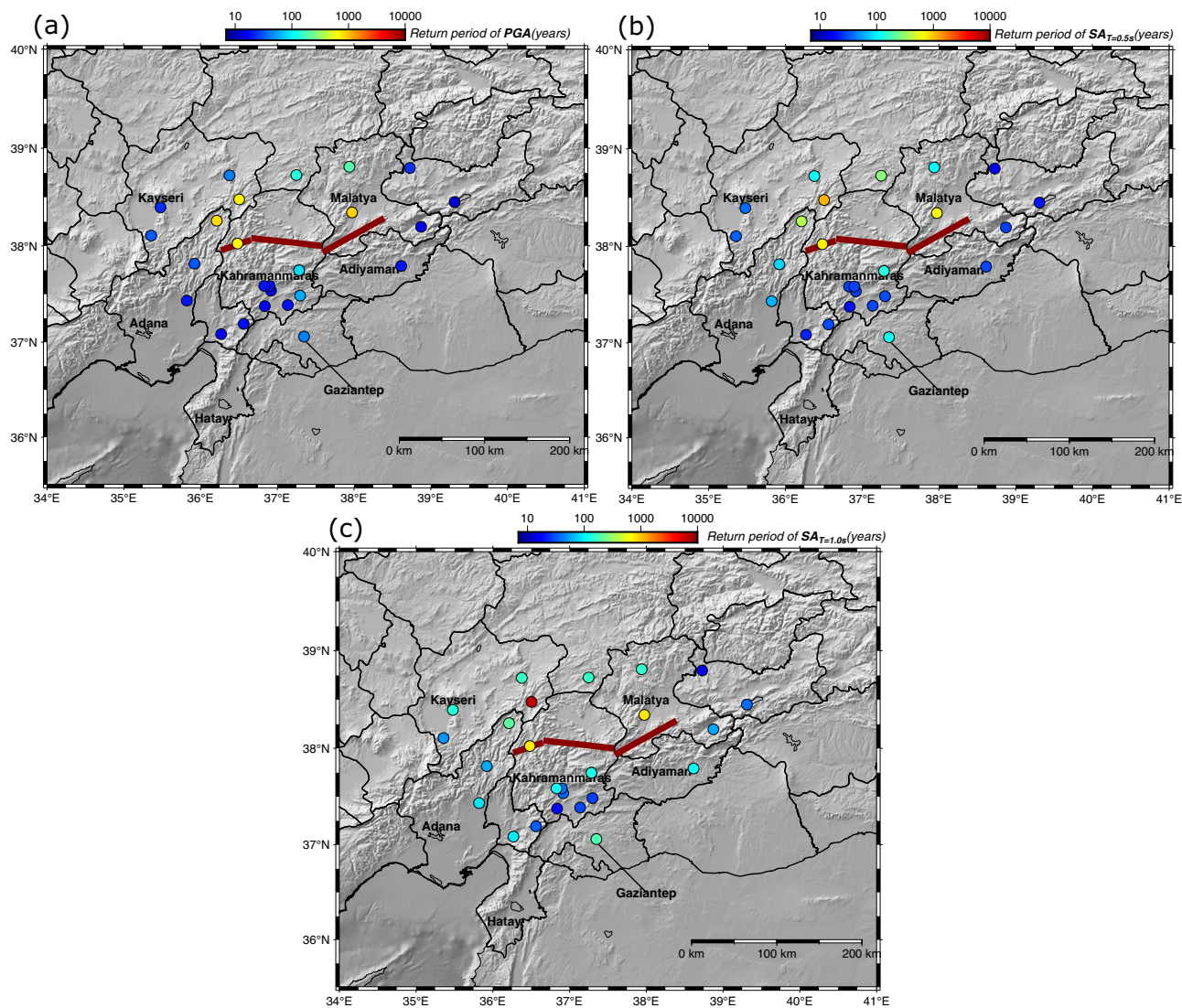
**Fig. 9 Maps showing the calculated mean return periods for the observed ground motion levels during the *Mw*7.5 Elbistan earthquake.** Maps show return periods of **a** *PGA*, **b** $SA_{T=0.5s}$, **c** $SA_{T=1.0s}$ for the *Mw*7.5 Elbistan earthquake.

Conversely, area sources are generally preferred where the fault structures are not very well known due to a lack of previous studies and historical large earthquakes in the vicinity. The fault source model yielded a mean return period of about 1000 years for the observed magnitude of 7.8 at EAFZ, whereas the two corresponding area sources yielded estimates between 3500-4000 years. For the Surgu and Cardak faults, the fault source model estimates a return period of 7800 years, whereas the area source model estimates 2600 years. In summary, the fault source model yields a lower estimate for the EAFZ, while the area source model yields a lower estimate for the Surgu and Cardak faults. This might indicate that fault sources work better in well-studied regions such as EAFZ. On the other hand, lack of information and higher epistemic uncertainty on fault geometry and seismicity at some sources might not allow accurate modeling and constraint of the source as a fault source model. This might be the case for the Surgu and Cardak faults, where the fault source model gives a very high mean return period of 7800 years.

The maximum amplitudes are generally recorded in Hatay during the *Mw*7.8 Pazarcik earthquake. Accordingly, the highest return periods are also estimated for Hatay, as the ground motions recorded at many stations in Hatay exceeded mean return periods of 1000 years. The high amplitudes in Hatay could

be attributed to rupture directivity effects, as most of the province is in the forward-directivity region. However, the concentration of high amplitude records in Hatay could also be related to the denser seismic network coverage, as the highest number of stations recording the *Mw*7.8 Pazarcik earthquake are also in Hatay in our dataset with 22 stations. After Hatay, the highest number of stations are in Kahramanmaras, with nine records, and there are no other provinces with more than five records in the dataset.

The *Mw*7.5 Elbistan earthquake was not as densely recorded as the *Mw*7.8 Pazarcik earthquake, with 25 records within 100 km rupture distance retained in our dataset. The highest amplitudes for this event are recorded in station 4612, in the Goksun district of Kahramanmaras, with *PGA*, $SA_{T=0.5s}$ and $SA_{T=1.0s}$ values of 0.58, 1.02, and 0.61 g, respectively. The mean return period estimates for these amplitudes are 750, 830, and 910 years for *PGA*, $SA_{T=0.5s}$ and $SA_{T=1.0s}$, respectively, for this station. Interestingly, these are not the highest return period estimates for this earthquake. For *PGA*, the highest return period is estimated for station 4406, located in Malatya, with 1250 years for the observed value of 0.44 g. For $SA_{T=0.5s}$ and $SA_{T=1.0s}$, highest return periods are estimated for station 3802 located in Kayseri for the observed values of 0.39 and 0.38 g, with 1600 and 6900 years, respectively. This discrepancy is due to Kayseri being located in a relatively
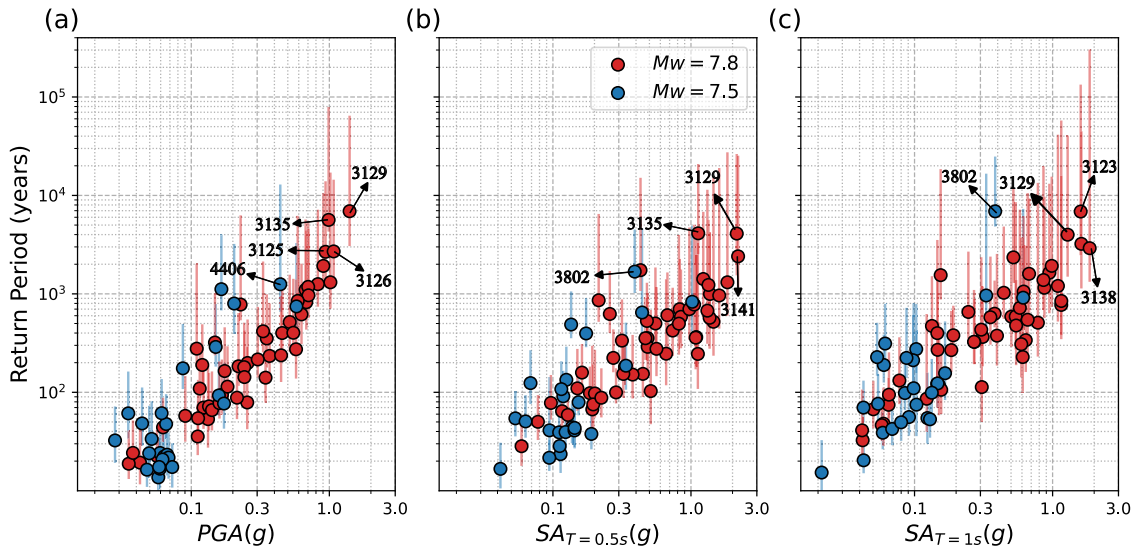
**Fig. 10 Estimated return periods plotted against the observed ground motion levels.** For **a** PGA, **b** $SA_{T=0.5s}$, **c** $SA_{T=1.0s}$. Stations at which some of the highest amplitudes are recorded or highest return periods are estimated are annotated. Red scatters show the data for the Mw7.8 Pazarcik earthquake, and blue scatters show the data for the Mw7.5 Elbistan earthquake. The lines passing through the scatters indicate the 16th and 84th percentile estimates.
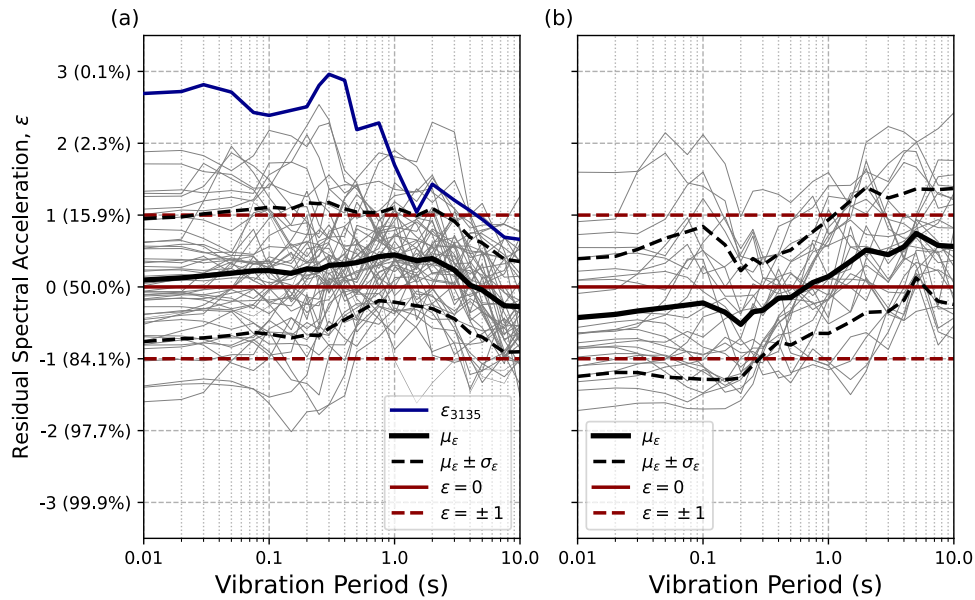


**Fig. 11 The normalized residual spectral acceleration ($\epsilon$) plotted against vibration periods between 0.01 and 10 seconds.** For **a** Mw7.8 Pazarcik earthquake, **b** Mw7.5 Elbistan earthquake. An individual record with very high $\epsilon$ values, recorded at station 3135 for the Mw7.8 Pazarcik earthquake is plotted in blue. The corresponding probability of exceedance values for $\epsilon$ values are given in parentheses.

low-hazard region. Still, station 3802 recorded considerably high amplitudes, especially at longer periods.

The standard residential buildings in Turkey are constructed for seismic loads corresponding to a return period of 475 years, determined according to TBEC[31] based on location and seismic site class. This return period is determined by assuming an average service time of 50 years for a building and aiming for a 10% probability of exceedance in those 50 years, assuming a Poisson distribution for exceedance rates. Similarly, return periods of 1000, 2500, 5000, and 10,000 years roughly correspond to the probability of exceedance values of 5%, 2%, 1%, and 0.05%, respectively, in a 50-year service time. The maximum return period estimates for the observed ground motions in these two earthquakes are about 7000 years, corresponding to a probability of exceedance value of 0.7% in 50 years. This implies that this

earthquake sequence simply resulted in much higher demands on structures compared to the levels they are designed for. However, these very high return periods (or low probabilities) should be interpreted very carefully and should not be thought to justify the observed widespread damage and losses. This study focused mostly on the most extreme motions recorded during the earthquake sequence. These few records can actually be considered local peaks of the spatial distribution of the motion. Therefore, the majority of the earthquake-affected region is actually thought to have experienced much lower ground shaking levels, which can also be inferred from the spatial distribution of peak ground motion parameters shown in Figs. 2 and 3.

When the behavior of residual spectral accelerations is investigated, it is observed that there is no apparent trend for the residuals of the Mw7.8 Pazarcik earthquake, meaning that
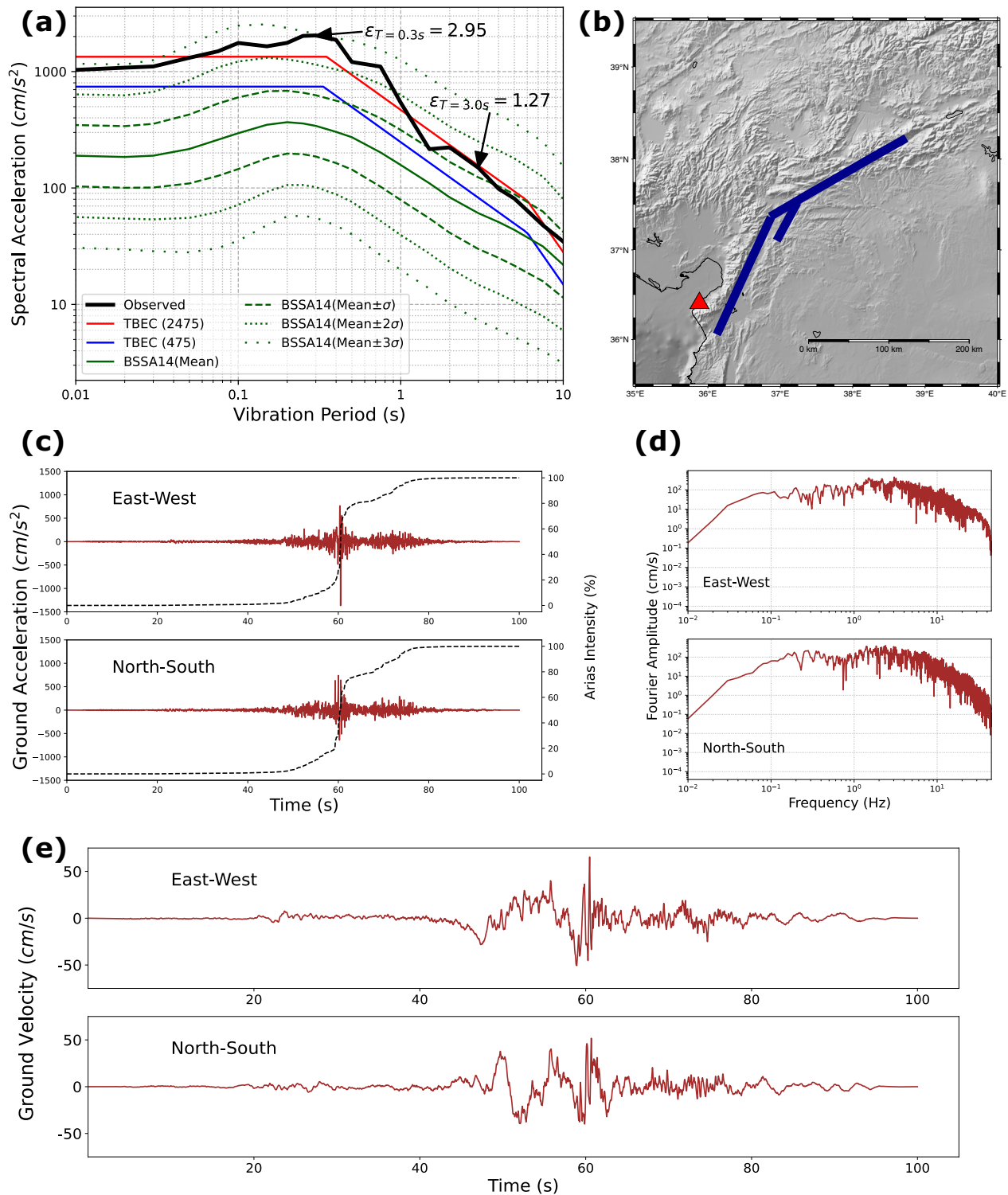
**Fig. 12 Investigation of the ground motion recorded at station 3135, located in Arsuz, Hatay. a** 5% damped elastic response spectrum of the ground motion. The response spectrum is compared to the 475- and 2475-year return period design spectra defined in Turkish Building Earthquake Code[31], and the GMM of Boore et al.[30]. **b** The location of station 3135 with respect to the fault rupture of the $Mw$7.8 Pazarcik earthquake. **c** Recorded ground accelerations at station 3135 for East–West and North–South components. Cumulative Arias intensity, i.e., Husid plot, is shown with the dashed line. **d** Fourier amplitude spectra of the recorded ground motions for East–West and North-South components. **e** Recorded ground velocity at station 3135 for East–West and North-South components.

the observed ground motions are generally in agreement with empirical models. However, some records have very high residuals across various periods (e.g., on stations 3126, 3129, 3135). For the $Mw$7.5 earthquake, a positive trend against the vibration period is observed for residuals, indicating substantial underestimation at longer periods.

Two stations in the compiled dataset for this study recorded spectral accelerations higher than the maximum values in the

**Table 2 A summary of ground motion records with the highest spectral acceleration values in the NGA-West2 database between discrete periods between 0.01 and 10 seconds.**

| Earthquake name | Earthquake ID | Record Sequence Number | Magnitude | Year | $R_{JB}$ (km) | $V_{S30}$ (m/s) |
|---|---|---|---|---|---|---|
| Nahanni, Canada | 97 | 495 | 6.76 | 1985 | 2.5 | 605 |
| Northridge-01 | 127 | 1051 | 6.69 | 1994 | 4.9 | 2016 |
| Northridge-01 | 127 | 1087 | 6.69 | 1994 | 0.4 | 257 |
| Kobe, Japan | 129 | 1120 | 6.9 | 1995 | 1.5 | 256 |
| Chi-Chi, Taiwan | 137 | 1231 | 7.62 | 1999 | 0.1 | 496 |
| Chi-Chi, Taiwan | 137 | 1517 | 7.62 | 1999 | 0.0 | 665 |
| Chi-Chi, Taiwan | 137 | 1503 | 7.62 | 1999 | 0.6 | 306 |
| Chi-Chi, Taiwan | 137 | 1505 | 7.62 | 1999 | 0.0 | 487 |
| Niigata, Japan | 180 | 4211 | 6.63 | 2004 | 10.2 | 419 |
| Niigata, Japan | 180 | 4209 | 6.63 | 2004 | 0.2 | 372 |
| Chuetsu-oki | 278 | 4894 | 6.8 | 2007 | 0.0 | 329 |
| Chuetsu-oki | 278 | 4856 | 6.8 | 2007 | 0.0 | 294 |
| Chuetsu-oki | 278 | 4875 | 6.8 | 2007 | 0.0 | 283 |
| Iwate | 279 | 5482 | 6.9 | 2008 | 13.1 | 459 |
| Iwate | 279 | 5657 | 6.9 | 2008 | 0.0 | 506 |
| Iwate | 279 | 5658 | 6.9 | 2008 | 6.0 | 371 |
| Wenchuan, China | 277 | 4816 | 7.9 | 2008 | 0.0 | 551 |
| Christchurch, New Zealand | 346 | 8158 | 6.2 | 2011 | 2.5 | 650 |
| Christchurch, New Zealand | 346 | 8157 | 6.2 | 2011 | 0.0 | 422 |
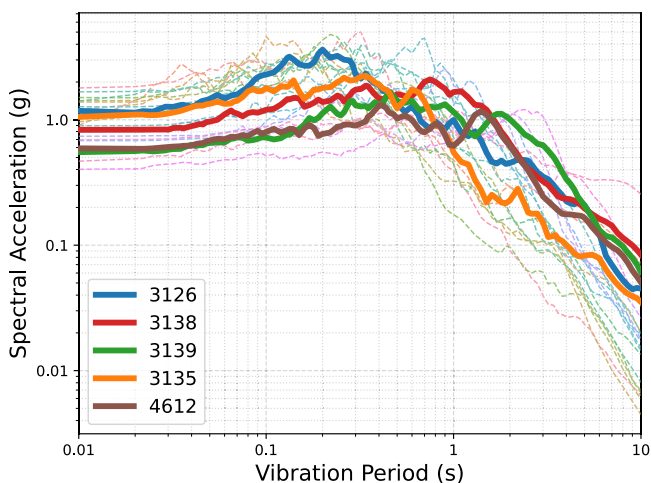


**Fig. 13 Comparison of the 5% damped elastic response spectra of five records from 6 February 2023 Kahramanmaras earthquakes against the records with the highest amplitudes in the NGA-West2 database.** Records at stations 3126, 3138, 3139, and 3135 are from the *Mw*7.8 Pazarcik earthquake. The record at station 4612 is from the *Mw*7.5 Elbistan earthquake. For the NGA-West2 database, records with maximum spectral acceleration values at discrete periods between 0.01 and 10 seconds are selected.

NGA-West2 database at periods of 1.5 and 1.8 seconds, roughly corresponding to the first mode periods of mid to high-rise reinforced concrete buildings. Since near-fault recordings of large-magnitude earthquakes are rare in recorded ground motion datasets, physics-based ground motion modeling might be preferred over empirical modeling for large earthquakes. Physics-based ground motion modeling might allow more accurate modeling of important physical phenomena, such as the effects of fault geometry, rupture directivity, rupture velocity, and long-period amplifications due to deep basins.

Recent advances in non-ergodic ground motion modeling are also promising tools for better ground motion estimation. In an ergodic process, the spatial variation of the variable is equivalent to its temporal variation, meaning that a model derived from observations at spatially distributed locations can approximate

the distribution over time at a single site. This assumption has to be made in generic ground motion modeling and PSHA due to the limited data in similar conditions repeating over time. However, with the increasing density of ground motion networks and number of observations, it is becoming more and more viable to develop non-ergodic GMMs to account for the site- and region-specific characteristics of ground motions[35,36]. These non-ergodic GMMs have the potential to estimate ground motions more accurately, especially with the increasing site- and region-specific ground motion data, by accounting for repeatable source, path, and site effects. However, most ground motion databases still lack near-fault records of large-magnitude events, which are generally the most critical scenarios for the seismic hazard assessment of sites located near active faults. Therefore, care must be taken to extrapolate these models to extreme conditions, such as imposing physical constraints for near-source magnitude scaling[35]. The large number of near-source observations from this earthquake sequence will likely lead to better characterization of ground motions from large magnitude earthquakes in ergodic ground motion modeling, as well as the estimation of ergodic terms for partially non-ergodic models. These potential improvements in ground motion modeling could yield much more robust hazard estimates in the future.

This study investigates the *Mw*7.8 Pazarcik and *Mw*7.5 Elbistan earthquakes and their ground motions separately. However, the Pazarcik earthquake most likely triggered the Elbistan earthquake, which occurred only nine hours later. Therefore, these two earthquakes are not statistically independent due to this triggering. Common practice PSHA does not consider triggering of secondary mainshocks or short-term clustering of large magnitude earthquakes. An active area of research, physics-based simulations of earthquake sequences, is a promising tool for modeling the complex behavior of fault ruptures, which can impose physical constraints on short-term clustering of large magnitude events and multi-segment fault ruptures in complex settings[37–45]. Incorporation of such models into PSHA might lead to much more accurate earthquake recurrence estimates.

One final note is necessary about the very high return periods estimated in this study, both for the earthquake recurrences and observed ground motion amplitudes. One of the biggest criticisms about the PSHA methodology is that the results are almost

impossible to validate or test practically (e.g., refs. [46,47]),. Although there are various studies on the validation of seismic hazard estimates against observations (e.g., refs. [48–52]), these validations are bound to be for short time windows. In particular, Beauval et al.[48] calculated the minimum required observation window to accurately calculate the mean return period of a Poisson process. They showed that a minimum observation window of 12,000 years is required for a return period of 475 years to ensure a coefficient of variation of 20% or less. Return periods of 3000 and 10,000 years require minimum time windows of 75,000 and 250,000 years, respectively, for the same threshold of 20% coefficient of variation. Consequently, the very high return periods estimated in this study contain substantial uncertainty and are likely sensitive to changes with improved modeling and longer instrumentation windows in the future. The return period estimates are also shown to be highly sensitive to input combinations in hazard calculations (see Fig. 7 and Fig. 10), highlighting the importance of accounting for the epistemic uncertainty in seismic hazard studies through the careful construction of logic trees.

## Data availability

## Code availability

## References

1. Ambraseys, N. N. Temporary seismic quiescence: SE Turkey. *Geophys. J. Int.* **96**, 311–331 (1989).
2. Westaway, R. & Arger, J. The Gölbasi basin, southeastern Turkey: a complex discontinuity in a major strike-slip fault zone. *J. Geol. Soc. London* **153**, 729–744 (1996).
3. Duman, T. Y. & Emre, Ö. The East Anatolian Fault: geometry, segmentation and jog characteristics. *Geol. Soc.* **372**, 495–529 (2013).
4. Emre, Ö. et al. Active fault database of Turkey. *Bull. Earthq. Eng.* **16**, 3229–3275 (2018).
5. Güvercin, S. E., Karabulut, H., Konca, A. Ö., Doğan, U. & Ergintav, S. Active seismotectonics of the East Anatolian Fault. *Geophys. J. Int.* **230**, 50–69 (2022).
6. Nalbant, S. S., McCloskey, J., Steacy, S. & Barka, A. A. Stress accumulation and increased seismic risk in eastern Turkey. *Earth Planet Sci. Lett.* **195**, 291–298 (2002).
7. Aktug, B. et al. Slip rates and seismic potential on the East Anatolian Fault System using an improved GPS velocity field. *J. Geodyn.* **94–95**, 1–12 (2016).
8. U.S. Geological Survey. *Finite Faults.* https://earthquake.usgs.gov/earthquakes/eventpage/us6000jllz/finite-fault (2023).
9. Gülerce, Z. et al. Probabilistic seismic-hazard assessment for east anatolian fault zone using planar fault source models. *Bull. Seismol. Soc. Am.* **107**, 2353–2366 (2017).
10. Gülerce, Z. et al. Preliminary Analysis of Strong Ground Motion Characteristics, February 6, 2023 Kahramanmaraş-Pazarcik (Mw=7.7) and Elbistan (Mw=7.5) Earthquakes. (2023). Available online https://eerc.metu.edu.tr/en/system/files/documents/CH4_Strong_Ground_Motion_Report_2023-02-20.pdf (Last accessed October 2023).
11. Akkar, S. et al. Reference database for seismic ground-motion in Europe (RESORCE). *Bull. Earthq. Eng.* **12**, 311–339 (2014).
12. Boore, D. M. Orientation-independent, nongeometric-mean measures of seismic intensity from two horizontal components of motion. *Bull. Seismol. Soc. Am.* **100**, 1830–1835 (2010).
13. Baker, J., Bradley, B. & Stafford, P. Seismic hazard and risk analysis. (Cambridge University Press, 2021). https://doi.org/10.1017/9781108425056.
14. Kramer, S. L. Geotechnical Earthquake Engineering. (Prentice-Hall Civil Engineering and Engineering Mechanics Series. Prentice Hall: Upper Saddle River, NJ, 1996).
15. McGuire, R. K. Seismic hazard and risk analysis. (Earthquake Engineering Research Institute, 2004).
16. Strasser, F. O., Bommer, J. J. & Abrahamson, N. A. Truncation of the distribution of ground-motion residuals. *J. Seismol.* **12**, 79–105 (2008).
17. Cosentino, P., Ficarra, V. & Luzio, D. Truncated exponential frequency-magnitude relationship in earthquake statistics. *Bull. Seismol. Soc. Am.* **67**, 1615–1623 (1977).
18. Youngs, R. R. & Coppersmith, K. J. Implications of fault slip rates and earthquake recurrence models to probabilistic seismic hazard estimates. *Bull. Seismol. Soc. Am.* **75**, 939–964 (1985).
19. Gutenberg, B. & Richter, C. F. Frequency of earthquakes in California. *Bull. Seismol. Soc. Am.* **34**, 185–188 (1944).
20. Danciu, L. et al. The 2020 update of the European Seismic Hazard Model-ESHM20: model overview. EFEHR Technical Report **1**, (2021).
21. Pagani, M. et al. OpenQuake engine: an open hazard (and risk) software for the global earthquake model. *Seismol. Res. Lett.* **85**, 692–702 (2014).
22. Kagan, Y. Y. Statistics of characteristic earthquakes. *Bull. Seismol. Soc. Am.* **83**, 7–24 (1993).
23. Utsu, T. Representation and analysis of the earthquake size distribution: a historical review and some new approaches. *In:* Seismicity Patterns, their Statistical Significance and Physical Meaning (eds. Wyss, M., Shimazaki, K. & Ito, A.) 509–535 (Birkhäuser Basel, 1999). https://doi.org/10.1007/978-3-0348-8677-2_15.
24. Basili, R. et al. European Fault-Source Model 2020 (EFSM20): online data on fault geometry and activity parameters. (2022).
25. Leonard, M. Self-consistent earthquake fault-scaling relations: update and extension to stable continental strike-slip faults. *Bull. Seismol. Soc. Am.* **104**, 2953–2965 (2014).
26. Kotha, S. R., Weatherill, G., Bindi, D. & Cotton, F. Near-source magnitude scaling of spectral accelerations: analysis and update of Kotha et al. (2020) model. *Bull. Earthq. Eng.* **20**, 1343–1370 (2022).
27. Kotha, S. R., Weatherill, G., Bindi, D. & Cotton, F. A regionally-adaptable ground-motion model for shallow crustal earthquakes in Europe. *Bull. Earthq. Eng.* **18**, 4091–4125 (2020).
28. Weatherill, G., Kotha, S. R. & Cotton, F. A regionally-adaptable "scaled backbone" ground motion logic tree for shallow seismicity in Europe: application to the 2020 European seismic hazard model. *Bull. Earthq. Eng.* **18**, 5087–5117 (2020).
29. Weatherill, G. & Cotton, F. A ground motion logic tree for seismic hazard analysis in the stable cratonic region of Europe: regionalisation, model selection and development of a scaled backbone approach. *Bull. Earthq. Eng.* **18**, 6119–6148 (2020).
30. Boore, D. M., Stewart, J. P., Seyhan, E. & Atkinson, G. M. NGA-West2 equations for predicting PGA, PGV, and 5% damped PSA for shallow crustal earthquakes. *Earthquake Spectra* **30**, 1057–1085 (2014).
31. TBEC, Turkish Building Earthquake Code. (2019).
32. Jayaram, N. & Baker, J. W. Statistical tests of the joint distribution of spectral acceleration values. *Bull. Seismol. Soc. Am.* **98**, 2231–2243 (2008).
33. Baker, J. W. & Jayaram, N. Correlation of spectral acceleration values from NGA ground motion models. *Earthquake Spectra* **24**, 299–317 (2008).
34. Ancheta, T. D. et al. NGA-West2 database. *Earthquake Spectra* **30**, 989–1005 (2014).
35. Lavrentiadis, G. et al. Overview and introduction to development of non-ergodic earthquake ground-motion models. *Bull. Earthq. Eng.* (2022) https://doi.org/10.1007/s10518-022-01485-x.
36. Kotha, S. R., Bindi, D. & Cotton, F. Partially non-ergodic region specific GMPE for Europe and Middle-East. *Bull. Earthq. Eng.* **14**, 1245–1263 (2016).
37. Yin, Y., Galvez, P., Heimisson, E. R. & Wiemer, S. The role of three-dimensional fault interactions in creating complex seismic sequences. *Earth Planet Sci. Lett.* **606**, 118056 (2023).
38. Field, E. H. How physics-based earthquake simulators might help improve earthquake forecasts. *Seismol. Res. Lett.* **90**, 467–472 (2019).
39. Field, E. H. et al. A spatiotemporal clustering model for the third uniform california earthquake rupture forecast (UCERF3-ETAS): toward an operational earthquake forecast. *Bull. Seismol. Soc. Am.* **107**, 1049–1081 (2017).
40. Shaw, B. E. et al. A physics-based earthquake simulator replicates seismic hazard statistics across California. *Sci. Adv.* **4**, eaau0688 (2023).
41. Milner, K. R., Shaw, B. E. & Field, E. H. Enumerating plausible multifault ruptures in complex fault systems with physical constraints. *Bull. Seismol. Soc. Am.* **112**, 1806–1824 (2022).

42. Lambert, V. & Lapusta, N. Resolving simulated sequences of earthquakes and fault interactions: implications for physics-based seismic hazard assessment. *J. Geophys. Res. Solid Earth* **126**, e2021JB022193 (2021).

43. Dal Zilio, L., Lapusta, N., Avouac, J.-P. & Gerya, T. Subduction earthquake sequences in a non-linear visco-elasto-plastic megathrust. *Geophys. J. Int.* **229**, 1098–1121 (2022).

44. Erickson, B. A. et al. Incorporating full elastodynamic effects and dipping fault geometries in community code verification exercises for simulations of earthquake sequences and aseismic slip (SEAS). *Bull. Seismol. Soc. Am.* **113**, 499–523 (2023).

45. Jiang, J. et al. Community-driven code comparisons for three-dimensional dynamic modeling of sequences of earthquakes and aseismic slip. *J. Geophys. Res. Solid Earth* **127**, e2021JB023519 (2022).

46. Stein, S., Geller, R. & Liu, M. Bad assumptions or bad luck: why earthquake hazard maps need objective testing. *Seismol. Res. Lett.* **82**, 623–626 (2011).

47. Gülkan, P. A dispassionate view of seismic-hazard assessment. *Seismol. Res. Lett.* **84**, 413–416 (2013).

48. Beauval, C., Bard, P.-Y., Hainzl, S. & Guéguen, P. Can strong-motion observations be used to constrain probabilistic seismic-hazard estimates? *Bull. Seismol. Soc. Am.* **98**, 509–520 (2008).

49. Ordaz, M. & Reyes, C. Earthquake hazard in Mexico City: observations versus computations. *Bull. Seismol. Soc. Am.* **89**, 1379–1383 (1999).

50. Gao, J., Tseng, Y. & Chan, C. Validation of the probabilistic seismic hazard assessment by the Taiwan earthquake model through comparison with strong ground motion observations. *Seismol. Res. Lett.* **93**, 2111–2125 (2022).

51. Mak, S. & Schorlemmer, D. A comparison between the forecast by the United States national seismic hazard maps with recent ground-motion records. *Bull. Seismol. Soc. Am.* **106**, 1817–1831 (2016).

52. Schorlemmer, D. & Gerstenberger, M. C. RELM testing center. *Seismol. Res. Lett.* **78**, 30–36 (2007).

53. Wessel, P. et al. The generic mapping tools version 6. *Geochem. Geophys. Geosyst.* **20**, 5556–5564 (2019).

54. Hunter, J. D. Matplotlib: a 2D graphics environment. *Comput. Sci. Eng.* **9**, 90–95 (2007).

## Acknowledgements

## Author contributions

A. Altindal performed the analyses and wrote the first draft of the manuscript. A. Askan supervised the analyses and edited the manuscript.

## Competing interests

The authors declare no competing interests.

## Additional information

**Supplementary information** The online version contains supplementary material available at https://doi.org/10.1038/s43247-023-01148-y.

**Correspondence** and requests for materials should be addressed to Abdullah Altindal.

**Peer review information** *Communications Earth & Environment* thanks Sreeram Reddy Kotha, Chung-Han Chan, and the other anonymous reviewer(s) for their contribution to the peer review of this work. Primary Handling Editors: Joe Aslin and Carolina Ortiz Guerrero. Peer reviewer reports are available.

**Reprints and permission information** is available at http://www.nature.com/reprints

**Publisher's note** Springer Nature remains neutral with regard to jurisdictional claims in published maps and institutional affiliations.